Electron transport through a metallic nanoparticle assembly embedded in SiO2 and SiNx by low energy ion implantation

Maxime Bayle, Jérémie Grisolia, Gérard Benassayag, Béatrice Pécassou, Caroline Bonafos, Patrizio Benzo, F. Gourbilleau, Robert Carles

Electron transport through a metallic nanoparticle assembly embedded in SiO_2 and SiN_x by low energy ion implantation

M. Bayle[1,2], J. Grisolia[*,1], G. Ben Assayag[2], B. Pecassou[2], C. Bonafos[2], P. Benzo[2,3], F. Gourbilleau[3], and R. Carles[2]

[1] Université de Toulouse, INSA-CNRS-UPS, LPCNO, 135 avenue de Rangueil, 31077 Toulouse, France
[2] CEMES-CNRS and Université de Toulouse, 29 rue Jeanne Marvig, BP 94347, 31055 Toulouse Cedex 4, France
[3] CIMAP, CNRS, CEA, ENSICAEN, UCBN, 6 Bd Marechal Juin, 14050 Caen Cedex, France

Keywords: electron transport in nanoscale materials, low energy ion implantation, nanoparticles

* Corresponding author: e-mail jeremie.grisolia@insa-toulouse.fr, Phone: +33 5 61 55 96 58, Fax: +33 5 61 55 96 97

Abstract

Original substrates have been developed to offer a new approach to modulate and analyse simultaneously electro-optical and transport properties through an assembly of metallic nanoparticles (NPs). Using low energy ion implantation, silver NPs have been synthesized at the vicinity of the free surface of a SiO_2 or SiN_x matrix. Varying the parameters of the process allows us to modify the density of NPs and their distance to the surface. While Ag NPs surface fraction in SiO_2 cannot exceed 20%, it reaches 30% in SiN_x. In the latter case, NPs with mean diameter is about 2.1 nm have an interdistance compatible with tunnel effect. We then developed devices that electrically address the embedded assembly of NPs for *I-V* characterization. The transport measurements on these devices show that an exploitable conduction is possible within the Ag NPs assembly in SiN_x. The Arrhenius-type temperature dependence model was successfully applied demonstrating that electron transport follows a simple thermally activated behaviour with the occurrence of a strongly localized regime.

1 Introduction

The understanding and control of electromagnetic interactions and charge transfer between a 2D electronic layer (e.g. graphene, dichalcogenide…) and an assembly of metallic nanoparticles (NPs) are of great interest for multiple electronic, optical or plasmonic applications [1–3]. So far, we have developed a specific architecture which consists of a plane of metallic NPs embedded at the vicinity of the free surface of a dielectric layer (Fig. 1) synthesized by low energy ion implantation [4]. 2D systems can be deposited on the surface and then interact with the NPs assembly that offers a new approach to modulate and analyse simultaneously electro-optical and transport properties. The most crucial parameter in this architecture, i.e. the distance between the NPs and 2D systems, can be finely controlled at the nanometer scale by using ion implantation at low kinetic energy. This accuracy allows a progressive tuning from electric field polarization to charge transfer for both transport properties and light scattering enhancement over a large perfectly flat area.

However, before developing any application it is necessary to check if the electrons are able to pass through the NPs assembly embedded in the dielectric matrix (e.g. SiO_2 or SiN_x). With this aim in mind, we varied the parameters of low energy ion implantation to tune the distance to the surface and more importantly to maximise the density of Ag nanoparticles embedded in SiO_2 or SiN_x.

We then developed devices that electrically address the embedded assembly of NPs. The transport measurements on these devices show that conduction is possible under certain conditions (mainly NPs density). Moreover, the *I-V* and *R-T* characteristic analyses provide the understanding of the physical mechanisms involved in the electron transport through such NPs metallic assemblies.

2 Experimental details

2.1 Ag nanoparticle synthesis

First, 240 nm thick SiO_2 layers were thermally grown on Si and 185 nm thick SiN_x layers were grown by reactive sputtering approach. Subsequently, low energy Ag^+ ions

were implanted in SiO_2 and SiN using 10 keV/1x10^{16} cm^{-2} and 20 keV/1.5x10^{16} cm^{-2}, respectively. The implantation has been carried out by means of a specifically modified Varian 200A2 implanter allowing to work in the low energy range, i.e. from 0.65 up to 20 keV with ion doses chosen to reach the higher density in the matrix. The ion current, which has a great influence on silver diffusion, has been kept constant at 5 µA during all the implantations [9–11]. Cross-sectional (XS) and plan-view (PV) samples were prepared for transmission electron microscopy (TEM) studies by the standard procedure involving grinding, dimpling, and Ar^+ ion beam thinning until electron transparency. Cooled ion milling has been used in order to avoid Ag diffusion and structure modification during sample preparation. A FEI Tecnai microscope equipped with a field emission gun and a spherical aberration corrector and operating at 200 keV was used for TEM analysis. TEM images of implanted layers are presented in Fig. 1. In both matrices, NPs form a 3D-dimensional assembly of NPs, few nanometers below the surface, but the density and the size of these NPs are very different in each case. In SiO_2, one can observe "big" NPs with a mean diameter D_{mean} = 4.6 nm and a surface fraction of 20%, whereas in SiN_x, the surface fraction reaches 30% with smaller NPs with D_{mean} = 2.1 nm. This behaviour is mainly due to the higher bulk density of SiN_x which limits the diffusion of Ag ions during the implantation process and leads to a higher implanted silver amount [4].

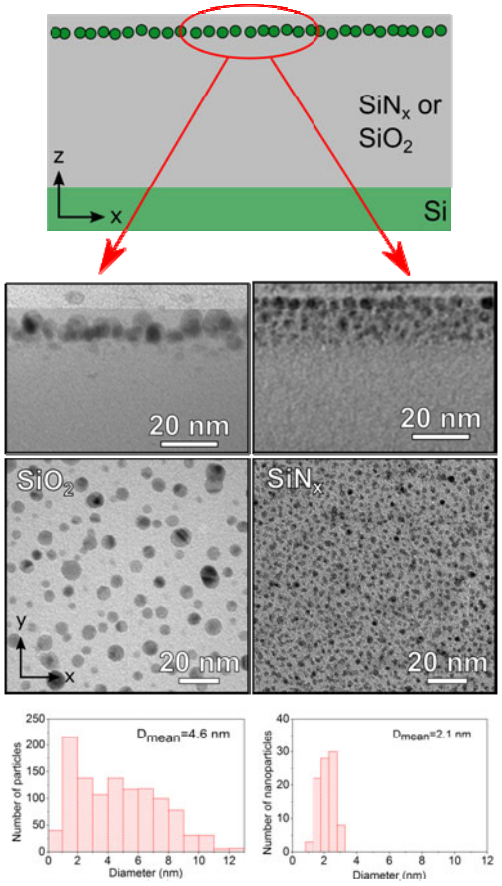

Figure 1 Schematic view of the nanocomposite heterostructure used, and TEM images with Ag NPs embedded in SiO_2 (left) or SiN_x (right), and their corresponding size distribution.

2.2 Device elaboration

After NPs synthesis in the matrix (SiO_2 or SiN_x) (Fig. 2a), electron transport devices were prepared following the subsequent processes: patterns of 150 nm (or 90 nm) thick SiO_2 (or SiN_x) layers were created by wet etching using buffered-HF (or H_3PO_4, respectively) solution (Fig. 2b), negative resist AZ5214 was then deposited and processed before depositing a 250 nm thick aluminium layer by reactive sputtering (Fig. 2c), lift off in acetone bath was used to remove the negative resist (Fig. 2d).

Figure 2e shows a TEM image of the device profile without any NPs in the SiO_2 matrix. This device was used as a reference. Preparation for TEM observation has been made on a specific area of the sample, with a special FIB technique [6].

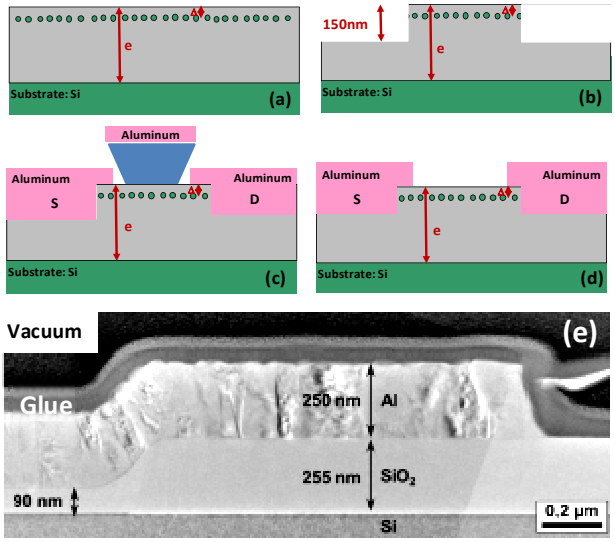

Figure 2 Steps of device process: (a) ion implantation inside the SiO_2 or SiN_x layer, (b) etching of 150 nm of the previous layers, (c) negative resist deposition and 250 nm-thick aluminum deposition, (d) negative resist lift off, and (e) image of the final profile of the device without any NPs in SiO_2 (control sample).

2.3 Device characterisation

The electrical properties of the devices have been measured using a Keithley 4200-SCS DC characterization system and a cryogenic probe station (Janis ST-500-1) operating under 10^{-5} mbar, in the temperature range of 77–300 K. The cooling rate was *ca.* 2.5 K/min. The Keithley 4200-SCS DC characterization system was equipped with a Keithley SMU pre-amp that gives a base level of approximately 1 fA with triax connections. *I-V* measurements were carried out by applying the voltage V in the form of sweeping pulses, while the current I was measured at each voltage step, ΔV after a delay time Δt, which gives an 'equivalent' sweep rate defined as $\Delta V/\Delta t$. All measurements were performed with a sweep rate of 0.1 Vs^{-1}. The measurements were conducted at different temperatures, through a step-wise decreasing cycle from T = 300 K to 77 K and by a step-wise increasing cycle from T = 77 K to 300 K at a rate of 0.05 K/s. More than 15 min delay was applied before any electrical measurement to let the system reach the thermal equilibrium. The temperature-dependent resistance *R-T* measurements were extracted at a given value in the low bias voltage of the *I-V* curves taken in the +/-10 V range.

3 Results and discussion

Figure 3 shows typical *I-V* characteristics of the SiO_2 samples during -10 V to 10 V measurements of 2 µm interelectrode distance. While the reference sample without NPs shows a resistance of tens of TΩ, the implanted one exhibits a ten times lower resistance. It is interestingly to note that the current shows several sharp peaks down-switching while no peak appears during the reverse sweeps (not shown here). Thus, the current peaks in the forward sweeps cannot be attributed to any resonant tunneling effect [7]. In this sample, the tunneling current does not pass uniformly through the whole NPs assembly, but through narrow leakage paths within the oxide. This is a reasonable assumption since the NPs assembly is largely disordered and has a huge interparticle distance distribution and structural size dispersion. "Charging centers", including NPs and oxide defects generated by ion implantation, located close to a current path can trap electrons. This locally leads to an electrostatic potential increase and the distribution of the electric field in the surrounding area is modified. As a result, the conductivity of this current path decreases. Similar behavior was previously found with Si NPs in SiO_2 synthesized by ultra low energy ion implantation [5] or 14 nm Au NPs with citrate ligands assembled on top of a SiO_2 layer [8].

Figure 3b presents how the current passing through the NPs assembly in SiN_x substrate is modified when varying the interelectrode distance L from 2 to 50 µm. The *I-V* characteristics exhibit both a highly nonlinear behavior and a much higher intensity (e.g. in the µA range below 10 V) with respect to the SiO_2 substrate. As the NPs sizes are relatively similar in SiO_2 and SiN_x layers, this current increase can be attributed to the increase of the surface fraction (> 30% in SiN_x and < 20% in SiO_2 layer) and also by the highest silver amount that probably leads during ion implantation to a higher defect density in the matrix [4]. It is interesting to note that no current peaks have been found in this sample. Moreover, these *I-V* characteristics show a strong dependence on the interelectrode distance L, i.e. on the number of tunneling junctions.

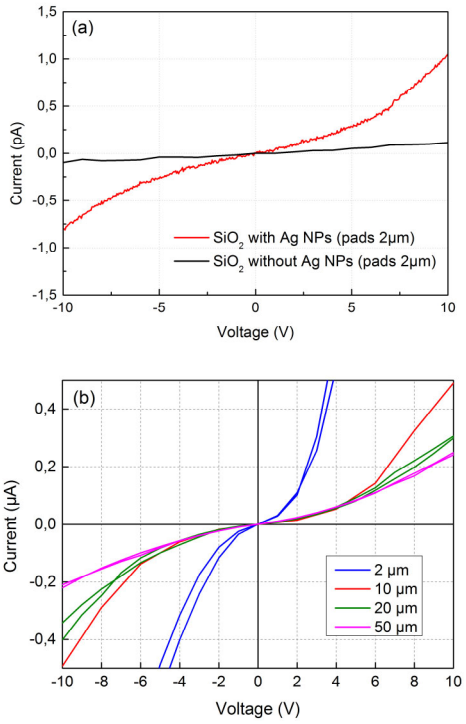

Figure 3 *I-V* characteristics at room temperature of Ag NP assemblies in (a) SiO_2 (for 2 µm interelectrode distance) and (b) SiN_x (for various interelectrode distances ranging from 2 µm to 50 µm).

3.1 Temperature-dependent electron transport

Temperature-dependent electric resistance measurements were performed to elucidate the electron transport mechanisms. Figure 4a shows that the low-bias resistance monotonously increases when temperature T decreases. The data are then consistent with tunneling transport through an array of metallic NPs in an insulating matrix, where the carrier density is activated with an activation energy given by the charging energy E_C.

Indeed, the tunneling current in a serie of tunnel junctions of small capacitance can be blocked by the charging effect at bias voltages eV that are below the Coulomb charging energy of a single electron defined as $E_C=e^2/2C$ where e is the electron charge and C stands for the capacitance the NPs assembly in its dielectric environment. This happens when E_C exceeds the energy of thermal and quantum fluctuations, $E_C > kT$ and $R_T > R_Q=h/4e^2$, where R_T is the where R_T is the tunneling resistance of one junction and R_Q the quantum resistance.

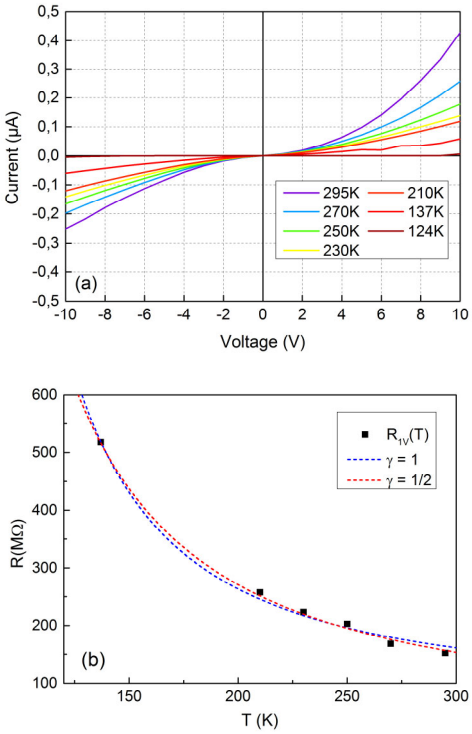

Figure 4 (a) *I-V* characteristics recorded for temperature ranging from $T = 120$ to 295 K for a 20 µm interelectrode distance, (b) resistance as a function of temperature at 1 V (blue and red curve represents respectively fitting with $\gamma = 1$ and $\gamma = 1/2$).

In order to determine the electron transport mechanisms we plotted the temperature dependence of R (Fig. 4b) extracted at a fixed low bias voltage of 1 V, which is inside the *I-V* gap.

3.2 Electron transport model analysis

The charge transport behaviors in nanocrystals assemblies reported so far often obeyed to the variable range hopping (VRH) model:

$$R \propto \exp[(T_0/T)^{\gamma}], \tag{1}$$

where T_0 is a constant and γ a value ranging from 0 to 1. Particularly, $\gamma = 1$ is for Arrhenius behavior and $\gamma = 1/2$ for non-Arrhenius behavior when strong Coulomb interactions exist. Theoretical modeling of electron transport behavior is made even more complicated since it can also combine these two behaviors [12]. In particular, the Efros-Shklovskii VRH (ES-VRH) model, developed for doped semi-conductors, that has $\gamma = 1/2$, describes the effect of balancing net tunnel distance and cost of energy.

As can be seen in Fig. 4b, the experimental results can be fitted (e.g. least squares method) with either $\gamma = 1$ or $\gamma = 1/2$. Therefore, it is difficult to determine which hopping mechanism dominates in this system. However, precise analysis of the charging energy and the localization lengths can help to elucidate the transport mechanism.

3.2.1 Arrhenius type temperature dependence ($\gamma = 1$)

In the Arrhenius regime the electrical resistance follows a simple thermally activated behavior, i.e. $\gamma = 1$, that give the subsequent zero-voltage resistance:

$$R \propto \exp\left[\left(\frac{E_a}{k_B T}\right)\right], \tag{2}$$

where E_a is the activation energy that represent a good estimation of the Coulomb charging energy E_C.

As shown in Fig. 4b, the *R-T* can obeyed to the Arrhenius-type temperature dependence with an activation energy ca. $E_C \sim 35$ meV determined by fitting the *R-T* curve. For an individual nanoparticle, this activation energy is strongly influenced by the particles size, the inter-nanoparticle distance, the dielectric constant of the surroundings, and the nearest-neighbor-number N. In the literature, studies that have examined the effect of the inter-particle distance on E_C value remain controversial since some report a small influence of the length of the ligand [17] while others infer a very strong influence [18]. These differences can arise from the models that are used to calculate the NP charging energy in assemblies. Most experiments consider the capacitance of an isolated sphere ([14–17, 20]):

$$C = 4\pi\varepsilon_0\varepsilon_r r \ , \tag{3}$$

where r is the radius of the NP, ε_0 is the vacuum permittivity, and ε_r is the relative dielectric constant of the matrix. Refined models were then proposed by Abeles *et al.* [21] by taking L_0 the inter-particle distance into account:

$$C = 4\pi\varepsilon_0\varepsilon_r r\left(\frac{r+L_0}{L_0}\right), \tag{4}$$

and by Beecher et al. (Eq. (5)) ([23, 24]):

$$C = 2N\pi\varepsilon_0\varepsilon_r r.ln\left(1+\frac{2r}{L_0}\right), \tag{5}$$

where N is the number of NPs surrounding a given particle (e.g. $N = 12$ and 6 for a 3D and 2D dense fcc packing respectively [22]) and L_0 the inter-particle distance.

In our case, the application of these models gives $E_C = e^2/2C$ values *ca.* 91 meV, 64 meV and 25 meV for isolated, Abeles and Beecher models respectively with diameter $d = 2r = 2.1$ nm and inter-nanoparticle distance $L_0 = 2.2$ nm, as extracted from TEM plan view image of Fig. 1 (right). One can observe that the most realistic model given the TEM observations is the Beecher et al. model which gives a theoretical value (25 meV) close to the experimental value extracted from the *R-T*, i.e. 35 meV. One can note that this latter value, that is higher than k_BT, is consistent with the observation of non-linear *I-V* characteristics.

3.2.2 ES-VRH temperature dependence (γ = 1/2)

Studying the applicability of ES-VRH model [19, 20] (γ = 1/2) requires an estimation of the localization length a, which is the reciprocal of the attenuation barrier β, and the hopping distance r_{hop} from the following equations:

$$R \propto \exp\left[\left(\frac{T_0^{ES}}{T}\right)^{\gamma}\right], \text{ where } T_0^{ES} = k\frac{e^2}{4\pi\varepsilon_0\varepsilon_r k_B a} \text{ and } a = \frac{1}{\beta}$$

$$\text{and } r_{hop} = \frac{1}{4\beta}\left(\frac{T_0^{ES}}{T}\right)^{1/2}. \quad (1)$$

The coefficient k, that depends on the assembly dimensionality ~ 6.5 (2D) and ~2.8 (3D) [13, 14] was fixed at 2.8 in agreement with the 3D-dimensional morphology of the NPs assembly (Figure 1). The decrease of the k value with decreasing dimensionality (e.g. from 3D to 2D) results from the higher energy barrier to establish percolating hopping paths through the assembly. Fitting the R-T curve at 1 V with Eq. (1) gives the values reported in Table 1.

Table 1 Electron transport parameters extracted from R-T fits using Eq. (4) for SiN_x sample.

	k	ε_r	T_0 (K)	a (nm)	β (nm^{-1})	r_{hop} (nm)
γ=1/2	2.8	7.5	1922	3.24	0.31	2.05

with γ = 1/2, the calculated localisation length from the fit is 3.24 nm is larger than the NPs diameter leading to an unreasonable physical value in this strongly localized regime. Hence, the application of the ES-VRH model to our samples yields unreasonable physically parameter values while Arrhenius-type dependent regime is consistent. In the frame of VRH model, this happens when the nearest neighbor hopping is favored.

4 Conclusion

We have developed devices that electrically address 3D Ag NPs assemblies embedded in SiO_2 and SiN_x by low energy implantation. While Ag NCs in SiO_2 have a 20% maximum surface fraction, this fraction reaches 30% in SiN_x due to its higher bulk density. In the latter case, the NPs whose mean diameter is ranging around 2.1 nm have an interdistance compatible with electron tunnelling. Transport measurements on these devices show that an exploitable conduction is only possible with Ag NPs assemblies in SiN_x. From I-V and R-T analysis we could provide the physical mechanisms involved in the electron transport through such 3D NPs metallic assemblies. The Arrhenius-type temperature dependence model was successfully applied demonstrating that electron transport follows a simple thermally activated behaviour with the occurrence of a strongly localized regime with a charging energy E_C ca. 35 meV. These results allow considering that such 3D assemblies of metallic NPs located ca. 2 nm below the free surface could be advantageously used to realize electrical and/or optical coupling in the near field regime with 2D layers such as graphene or dichalcogenides deposited on this surface.

Acknowledgements This study has been (partially) supported through the grant NEXT No. ANR-10-LABX-0037 in the framework of the "Programme des Investissements d'Avenir". M.B. thanks the University of Toulouse and the Région Midi-Pyrénées for financial support.

References

[1] P. Avouris et al., Nano Lett. **10**, 4285 (2010).
[2] C. Soldano et al., Carbon **48**, 2127 (2010).
[3] T. Verawati et al., J. Mater. Chem. **21**, 15593 (2011).
[4] P. Benzo et al., J. Appl. Phys. **113**, 193505 (2013).
[5] M. Shalchian, J. Grisolia, G. Ben Assayag, H. Coffin, S. M. Atarodi, and A.Claverie, Appl. Phys. Lett. **86**, 163111, (2005).
[6] D. Cooper, C. Ailliot, J.-P. Barnes, J.-M. Hartmann, P. Salles, G. Benassayag, and R. E. Dunin-Borkowski, Ultramicroscopy **110,** 383 (2010).
[7] L.L. Chang, E.E. Mendez, and C. Tejedor (eds.), Resonant Tunneling in Semiconductors: Physics and Applications, NATO ASI Series, Ser. B: Physics, Vol. 277 (Plenum Press, N.Y., 1991). pp. 505-513.
[8] J. Grisolia, B Viallet, C. Amiens, S. Baster, A. S. Cordan, Y. Leroy, C. Soldano, J. Brugger, and L. Ressier Nanotechnology **20**, 355303 (2009).
[9] A. L. Stepanov, Rev. Adv. Mater. Sci. **26**, 1 (2010).
[10] A. L. Stepanov, V. A. Zhikharev, D. E. Hole, P. D. Townsend, and I. B. Khaibullin, Nucl. Instrum. Methods Phys. Res. B **166-167**, 26 (2000).
[11] A. L. Stepanov and V. N. Popok, Tech. Phys. Lett. **29**, 977 (2003).
[12] K.-H. Müller and M. M. A. Yajadda J. Appl. Phys. **111**, 123705 (2012); doi: 10.1063/1.4729491.
[13] K. Xu, L. Qin, and J. R. Heath, Nature Nanotechnol. **4**, 368 (2009).
[14] T. B. Tran, I. S. Beloborodov, J. Hu, X. M. Lin, T. F. Rosenbaum, and H. M. Jaeger, Phys. Rev. B **78**, 075437 (2008).
[15] Y. Noda, S. Noro, T. Akutagawa, and T. Nakamura, Phys. Rev. B **82**, 205420 (2010).
[16] M. S. Kang, A. Sahu, D. J. Norris, and C. D. Frisbie, Nano Lett. **11**, 3887 (2011).
[17] H. Moreira, Q. Yu, B. Nadal, B. Bresson, M. Rosticher, N. Lequeux, A. Zimmers, and H. Aubin, Phys. Rev. Lett. **107**, 176803 (2011)
[18] J. Dugay, R. P. Tan, M. Ibrahim, C. Garcia, J. Carrey, L.-M. Lacroix, P.-F. Fazzini, G. Viau, and M. Respaud, Phys. Rev. B **89**, 041406(R) (2014).
[19] A. L. Efros and B. I. Shklovskii, J. Phys. C **8**, L49 (1975); B.I. Shklovskii and A.L. Efros, Electronic Properties of Doped Semiconductors (Springer-Verlag, Berlin, 1988).
[20] D. Yu, C. Wang, B. L. Wehrenberg, and P. Guyot-Sionnest, Phys. Rev. Lett. **92**, 216802 (2004).
[21] B. Abeles, P. Sheng, M. Coutts, and Y. Arie, Adv. Phys. **24**, 407 (1975).
[22] Y. Wang, C. Duan, L. Peng, and J. Liao, Sci.: Rep. **4**, 7565 (2014).
[23] P. Beecher, A. J. Quinn, E. V. Shevchenko, H. Weller, and G. Redmond, Nano Lett. **4**, 1289 (2004).
[24] C. T. Black, C. B. Murray, R. L. Sandstrom, and S. Sun, Science **290**, 1131 (2000).